THE $^{12}C(\alpha, \gamma)^{16}O$ CROSS SECTION AT STELLAR ENERGIES*

A. REDDER, H.W. BECKER, C. ROLFS and H.P. TRAUTVETTER

Institut für Kernphysik, Universität Münster, Münster, W. Germany

T.R. DONOGHUE and T.C. RINCKEL

The Ohio State University, Columbus, Ohio, USA

J. W. HAMMER

Institut für Strahlenphysik, Universität Stuttgart, Stuttgart, W. Germany

K. LANGANKE

Institut für Theoretische Physik, Universität Münster, Münster, W. Germany

Abstract: The capture reaction $^{12}C(\alpha, \gamma)^{16}O$ has been investigated at $E = 0.94$ to 2.84 MeV with the use of an intense α beam and implanted ^{12}C targets of high isotopic purity. The studies involved NaI(Tl) crystals and, for the first time, germanium detectors. The measurement of absolute cross sections, γ-ray angular distributions and excitation functions is reported. A cross section of 48 pb is found at $E = 0.94$ MeV. The data provide information on the E1 and E2 capture amplitudes involved in the transition to the ground state as well as to excited states. The S-factor at stellar energies has been determined by means of theoretical fits. The results verify the previous report of a substantial higher S-value compared to the value recommended in 1975. The present uncertainty in the S-value as well as possible improvements are discussed. This S-value is of crucial importance to nuclear astrophysics.

1. Introduction

The $^{12}C(\alpha, \gamma)^{16}O$ reaction (fig. 1) is one of the most important processes in nuclear astrophysics [1]. It influences [2,3] sensitively the predicted abundance distribution of the elements between carbon and iron. Even more subtle, however, is its effect [3] on the structure of supernova models affecting both the explosion mechanism and the mass range of compact remnants. Enormous experimental efforts [4-6] have gone into studies of this capture reaction, where formidable problems are encountered. The problems arise from the combination of a low γ-ray capture yield, in the nanobarn and subnanobarn region, and a high neutron-induced γ-ray background
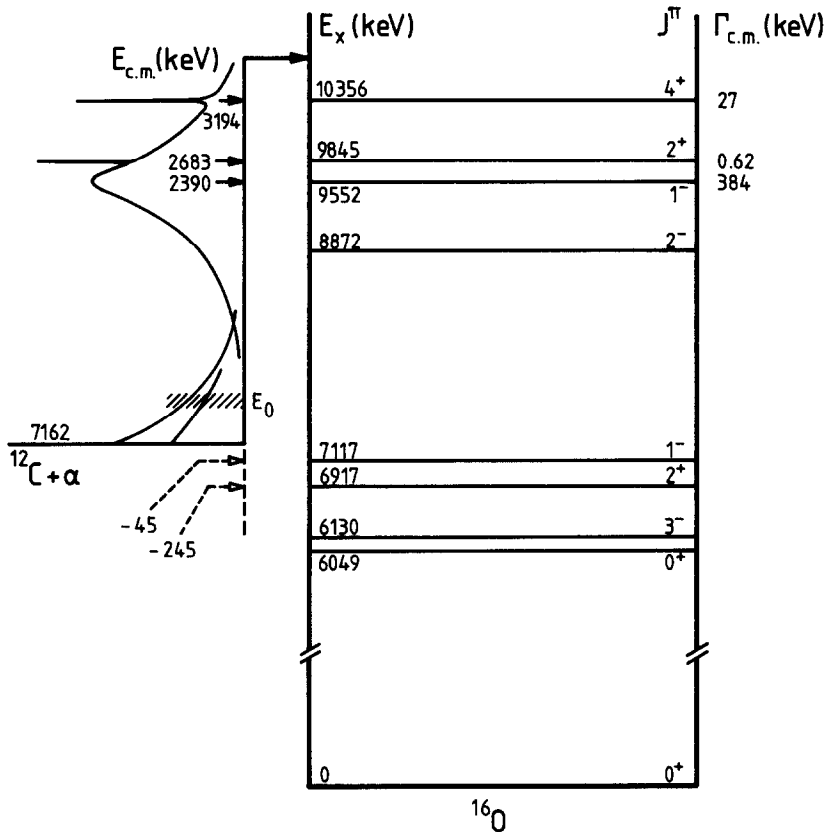
Fig. 1. Level scheme of ^{16}O near and above the α-particle threshold [11,26]. In the astrophysically important energy region near $E_0 = 0.3$ MeV, the $^{12}C(\alpha, \gamma)^{16}O$ reaction yield (shown schematically in form of the $S(E)$ factor) appears to be dominated by the high-energy wings of two subthreshold resonances, at $E_R = -45$ and -245 keV.

arising mainly from the $^{13}C(\alpha, n)^{16}O$ reaction. As a consequence, measurements were carried out using targets of high ^{12}C isotopic purity and time-of-flight techniques [4,5]. In another experiment [6] the neutron-induced γ-ray background from the $^{13}C(\alpha, n)^{16}O$ reaction was eliminated by interchanging the role of projectiles and target nuclei, i.e., the ^4He target nuclei contained in a windowless gas target were bombarded with an intense ^{12}C beam. In the work of Dyer and Barnes [5] the γ-ray detector was placed, for the most part, at $\theta_\gamma = 90°$ and thus only the E1 portion of the capture cross sections was reported. In the work of Kettner et al. [6] the detectors were placed in close geometry to the target resulting in angle-integrated total capture cross sections. In spite of these efforts, there are still considerable uncertainties in the cross section at the relevant stellar energy of 0.3 MeV. The principal uncertainty arises from differences in extrapolation of higher-energy cross-section data to stellar energies. As a result, the astrophysical S-factor at 0.3 MeV

determined by Kettner *et al.*[6]) is some fourfold higher than that obtained[7]) from the data of Dyer and Barnes[5]). Since the absolute cross sections, near the maximum of the $E_R = 2.39$ MeV* $(J^\pi = 1^-)$ resonance (fig. 1), between the two data sets differ only by about 25% (sect. 3.1), it has been suggested[6]) that the above discrepancy might lie to a large extent in the difference between the partial (E1) and the total (E1 + E2) capture yields. The finding of a nonnegligible E2 capture amplitude at stellar energies[6]) has been supported by recent microscopic-model calculations[8-10]). A major difficulty in determining the relative and absolute amounts of both the E1 and E2 capture amplitudes arises because the cross section at 0.3 MeV appears to be influenced strongly by the high-energy wings of two ^{16}O states[11]), at $E_x(J^\pi) =$ 6917 (2^+) and 7117 (1^-) keV, corresponding to subthreshold resonances at $E_R = -245$ and -45 keV, respectively (fig. 1). Thus, their observation necessitates direct measurements of the reaction $^{12}C(\alpha, \gamma)^{16}O$ at energies far below the Coulomb barrier. To improve the information on the relative and absolute amplitudes of both multipole transitions, measurements of γ-ray angular distributions are required over a wide range of α-energies, including as low an energy as is technically possible. Such measurements are reported here. Preliminary results have been reported[12]) and are superseded by the present work. The measurement of absolute cross sections and excitation functions is also reported.

2. Experimental equipment and set-up

Preliminary investigations demonstrated that the measurement of γ-ray angular distributions at subcoulomb energies required the use of (i) high α-beam currents and (ii) ^{12}C targets depleted in ^{13}C to reduce the neutron-induced background and capable of withstanding these currents.

The 4 MV Dynamitron accelerator at Stuttgart[13,14]) provided an α-beam of 200-700 μA in the energy range of $E_\alpha = 1.3$-3.9 MeV. The energy calibration of the beam analyzing magnet[14]) was checked in the present work at the narrow $E_R = 2.68$ MeV resonance of $^{12}C(\alpha, \gamma)^{16}O$ as well as at the $E_R = 957$ keV resonance of $^{27}Al(p, \gamma)^{28}Si$. The beam was directed into a cylindrical target chamber[15]) through beam-defining collimators and liquid-nitrogen shrouds and defocused on the target to a beam spot of about 15 mm diameter. The target together with the target chamber constituted the Faraday cup for beam current integration[15]). A negative voltage was applied to the shroud to minimize the effects of secondary electrons.

The ^{12}C targets were produced[15,16]) by ion implantation into a gold layer, which had been evaporated onto a 2 mm thick Cu sheet $(2 \times 2$ cm^2 area). The Cu backing[17]) has fourteen 1 mm diameter channels for cooling the target with water at 50 bar pressure. The Cu backing was soldered on two stainless steel tubes for the water inlet and outlet. The gold layer, bonded to the Cu with a thin Ni layer, had a thickness equal to the range of a 4 MeV α-particle. Each target contained about 2

---

* Throughout this work, all energies are in the c.m. system, except where quoted.

coulombs of ^{12}C ions implanted in Au with a 110 keV beam from the 350 kV Münster accelerator. During implantation, the ^{12}C beam was scanned over the full area of the target. Several liquid-nitrogen shrouds in the beam line minimized [16]) the usual carbon deposition on the target during implantation to a negligible level. The content and distribution of the implanted ^{12}C zone was determined [15,16]) in situ by use of the ^{12}C(p, γ)^{13}N reaction [18]) as well as during the ^{12}C(α, γ)^{16}O studies by use of the narrow $E_R = 2.68$ MeV resonance. It was found that the ^{12}C targets started at the surface of the Au layer and had a nearly homogeneous distribution, with ^{12}C-to-Au abundance ratios of about 5. Targets of thicknesses of about 80 keV at $E = 2.68$ MeV have been produced [15]), consistent with the range of the implanted ^{12}C ions. The resulting targets had a ^{13}C depletion of about two orders of magnitude compared to a standard carbon target (isotopic ratio ^{13}C/^{12}C $\simeq 10^{-4}$), a limit set by the mass resolution of the Münster accelerator facility [16]). The depletion was sufficiently low to reduce significantly the neutron-induced background (fig. 2) as well as to allow safe use of Ge(Li) detectors (fig. 3). The targets withstood beam loads of up to 0.5 kW for about 100 h without significant deterioration (for higher beam loads, see sect. 3.2). With the use of several liquid-nitrogen shrouds in the beam line no carbon buildup on the target during bombardment was observed [15]).

Gamma-ray angular distributions were measured with NaI(Tl) crystals as well as with germanium detectors. In a first experiment, 8 crystals were used which had all nearly the same size (7 crystals with 10.2 cm $\varnothing$ × 10.2 cm and 1 crystal with 12.7 cm $\varnothing$ × 12.7 cm). They were placed at such distances from the target ($d = 13.5$ and 16.9 cm) that the attenuation coefficients Q_k were similar. The crystals were located at angles of 15°, 30°, 60°, 75°, 90°, 105°, 120°, and 150°. In a second experiment, 6 germanium detectors of 12 to 35% efficiency were placed at a distance of 8 cm from the target and at angles of 15°, 40°, 60°, 90°, 120°, and 150°. In a third experiment, 3 germanium detectors were placed closer to the target ($d = 5$-6 cm) at angle of 15°, 90°, and 120°. The data from this latter experiment extended over the widest energy range – and to as low as $E = 0.94$ MeV – and were used in the determination of excitation functions. The relative and absolute efficiency η_γ of these detector arrangements was determined [15]) with radioactive sources and with γ-rays from the ^{27}Al(p, γ)^{28}Si capture reaction [19]) at $E_R = 957$ keV ($E_\gamma = 0.5$–10.8 MeV). For the germanium detectors, the number of counts in the full-energy, one-escape, and double-escape peaks of each capture γ-ray transition (fig. 3) was corrected for the relative efficiencies and then summed.

3. Experimental procedures, data analyses and results

3.1. ABSOLUTE CROSS SECTION

In the course of angular distribution measurements using 6 germanium detectors (second experiment), the absolute cross section σ for ^{12}C(α, γ_0)^{16}O at $E = 2.26$ and
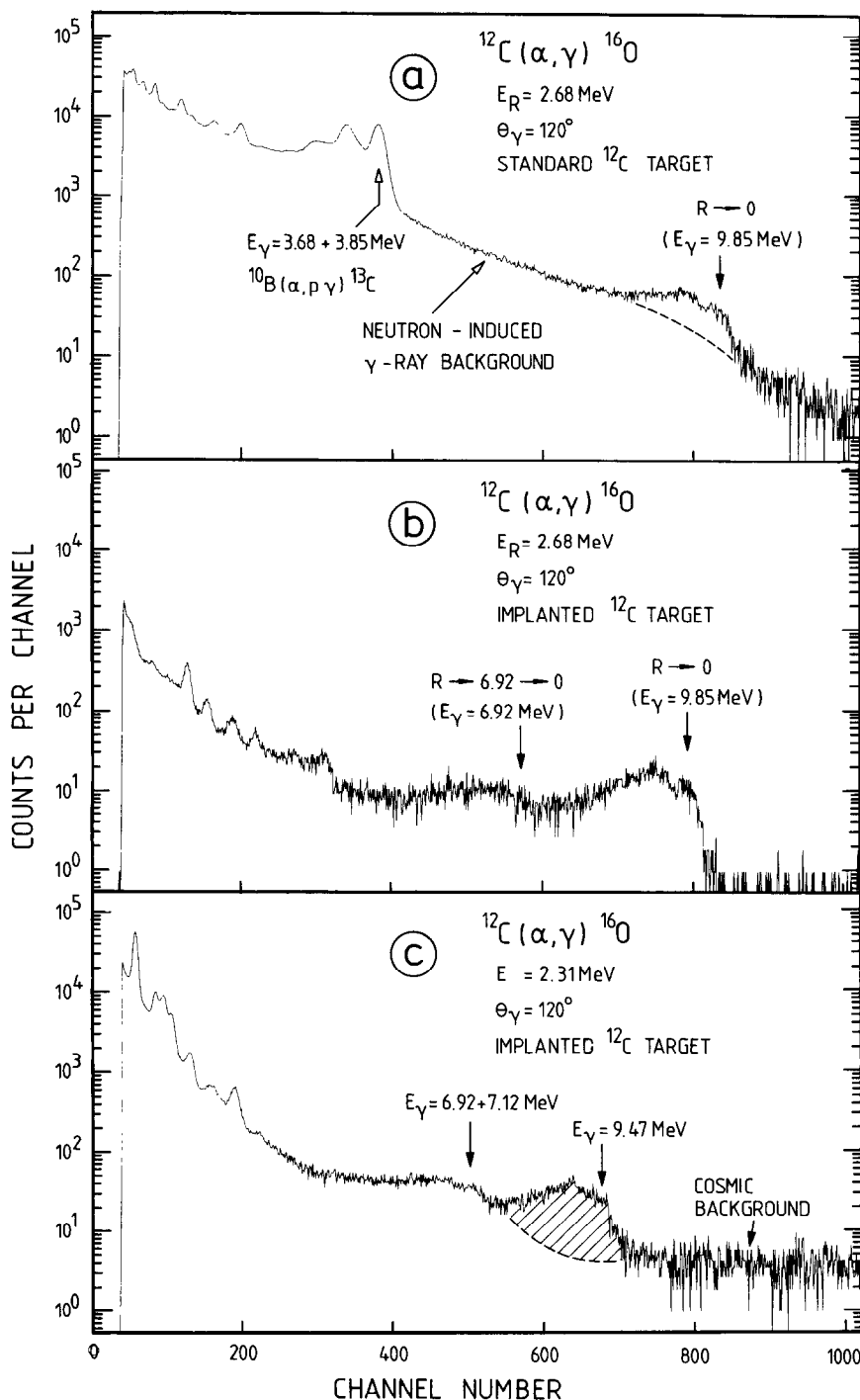
Fig. 2. Gamma-ray spectra obtained with a NaI(Tl) crystal at the strong and narrow resonance at $E_R = 2.68$ MeV using (a) a standard target of normal isotopic composition and (b) an implanted ^{12}C target. A significant improvement in the signal-to-noise ratio for the capture transitions is noted. At energies away from this resonance, the capture cross section is much smaller and the analysis of the γ_0 ray intensity (shaded area in (c)) depends to some extent on the assumption of background subtraction.
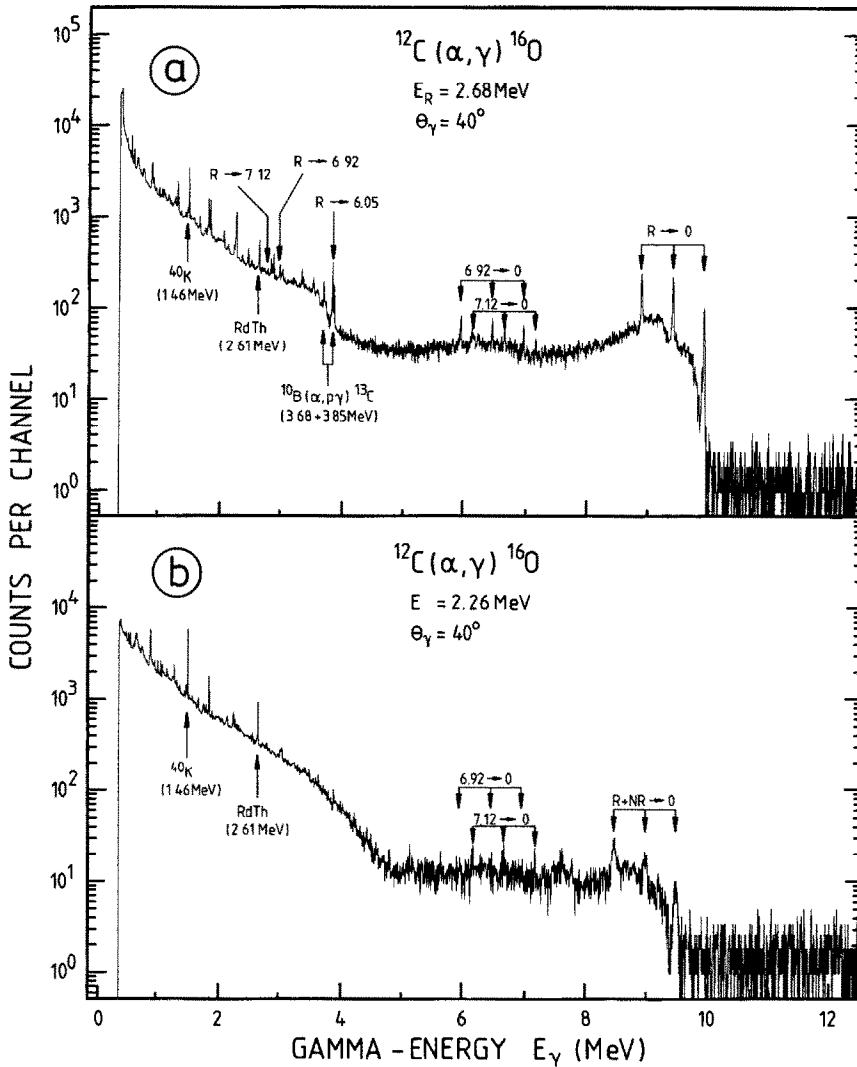
Fig. 3. Gamma-ray spectra obtained with a germanium detector and an implanted ^{12}C target at (a) the narrow $E_R = 2.68$ MeV resonance and (b) at $E = 2.26$ MeV. The widths of the full-energy, one-escape, and double-escape peaks of the ground-state transition in (b) reflect the target thickness. Also shown in (a) are the primary transitions $R \to 6.05$, $R \to 6.92$ and $R \to 7.12$ MeV as well as the $6.92 \to 0$ and $7.12 \to 0$ MeV secondary transitions at the 2.68 MeV resonance. At the other energies (b) only the secondary transitions $6.92 \to 0$ and $7.12 \to 0$ MeV could be observed. The origin of some low-energy background lines is also given.

2.36 MeV was obtained via the relation

$$N_\gamma = N_\alpha N_t \eta_\gamma \sigma$$

where N_γ represents the angle-integrated number of counts for the γ_0 ray transition and N_α the number of incident α-particles. The number of ^{12}C atoms per cm^2, N_t, in the implanted target (I) was obtained relative to that in a standard evaporated target of normal isotopic composition (S) by γ-ray yield comparisons of the $^{12}C(p, \gamma_0)^{13}N$ reaction at $E_p = 1.20$ MeV:

$$N_\gamma(S)/N_\gamma(I) = N_t(S)/N_t(I) = \Delta(S)/(N_t(I)\varepsilon(S)) .$$

The c.m. target thickness $\Delta(S)$ of the standard carbon target was measured [15] via the energetic width of the capture γ_0 ray transition and the c.m. stopping power $\varepsilon(S)$ was derived from recent compilations [20]. The combined results are $\sigma = 46 \pm 6$ nb at $E = 2.36$ MeV. The quoted uncertainty was obtained by the quadratic addition of errors in N_γ (2%), N_α (5%), N_t (8%), and η_γ (8%).

A second cross section value was obtained relative to the γ_0 ray strength of the $E_R = 2.68$ MeV narrow resonance [11] with $\omega\gamma = 29.5 \pm 3.0$ meV. The thick-target yield at this resonance and the non-resonant yield at $E = 2.36$ MeV are related by

$$\frac{N_\gamma(E_R)}{N_\gamma(E)} = \frac{N_\alpha(E_R)}{N_\alpha(E)} \frac{\eta_\gamma(E_R)}{\eta_\gamma(E)} \frac{\omega\gamma}{\Delta(E_R)} \frac{\lambda^2(E_R)}{2\sigma(E)} ,$$

where $\Delta(E_R)$ is obtained from the thick-target yield curve at E_R. The quantities $N_\gamma(E_R)$ and $N_\gamma(E)$ represent angle-integrated γ-ray fluxes. The resulting value of $\sigma = 47 \pm 6$ nb together with the above result led to the weighted average of $\sigma = 46 \pm 4$ nb at $E = 2.36$ MeV. This value is in fair agreement with the result of Kettner et al. [6] ($\sigma = 53 \pm 4$ nb at $E = 2.40$ MeV) and that of Dyer and Barnes [5] ($\sigma = 42 \pm 4$ nb at $E = 2.32$ MeV, where an additional E2 contribution of about 5% (fig. 6) has been added to the reported E1 capture data). The weighted average of $\sigma = 47 \pm 3$ nb has been adopted as the standard for the $^{12}C(\alpha, \gamma_0)^{16}O$ reaction. For a comparison of excitation functions between previous and present work as well as for extrapolation of the data to stellar energies, the absolute cross sections from previous work [5,6] have been normalized to the above standard. The reported data of Jaszczak et al. [4] have not been used since it is not clear whether they represent E1 capture only.

3.2. EXCITATION FUNCTION FOR THE E1 CAPTURE CROSS SECTION

The γ_0 ray angular distribution $W(\theta_\gamma)$ for E1 capture is described [21] by the pattern $\sin^2 \theta_\gamma$ and that for E2 capture by $\sin^2 \theta_\gamma \cos^2 \theta_\gamma$. As a consequence, at $\theta_\gamma = 90°$ only the E1 capture process is detectable and the observed yield is independent [21] of the E2 capture process as well as of possible E1–E2 interference effects (sect. 3.3). The exception to these statements arises from the finite size of the

germanium detector ($Q_2 = 0.92$ and $Q_4 = 0.75$) leading to a relatively small correction [15]), e.g., of about 13% for a ratio of $\sigma_{E2}/\sigma_{E1} = 1$ (fig. 6). Aside from this correction, angle-integrated E1 capture cross sections are derived from the 90° γ-ray data using the ratio $W(\theta_\gamma = 55°)/W(\theta_\gamma = 90°) = \frac{2}{3}$.

An excitation function was obtained (third experiment) in the energy range of $E = 0.94$–2.84 MeV. The lowest data point was obtained with an accumulated charge of 287 coulombs. The effective energy E within the target was determined by the centroids of the γ_0 ray lines (e.g., fig. 3b), corrected for Doppler effects, where the energy calibration of the detectors was obtained at the $E_R = 2.68$ MeV resonance. This narrow resonance was also used periodically throughout the experiments to test the quality of the targets [15]) (thickness and yield). At the lowest energies high α currents (500 to 700 μA) were used and the targets exhibited thus a 10% deterioration (probably via sputtering effects) after 3 to 4 days of beam loads. The damaged target was then replaced by a nearly identical target. The E1 capture yields, corrected for variations in target thickness and in γ-ray efficiency, are displayed in fig. 4 (and summarized in table 1) in form of the astrophysical S-factor defined as

$$S(E) = E\sigma(E) \exp(2\pi\eta)$$

with $2\pi\eta = 650.51/E^{1/2}$ and with E in keV. Also shown in fig. 4 are the E1 capture
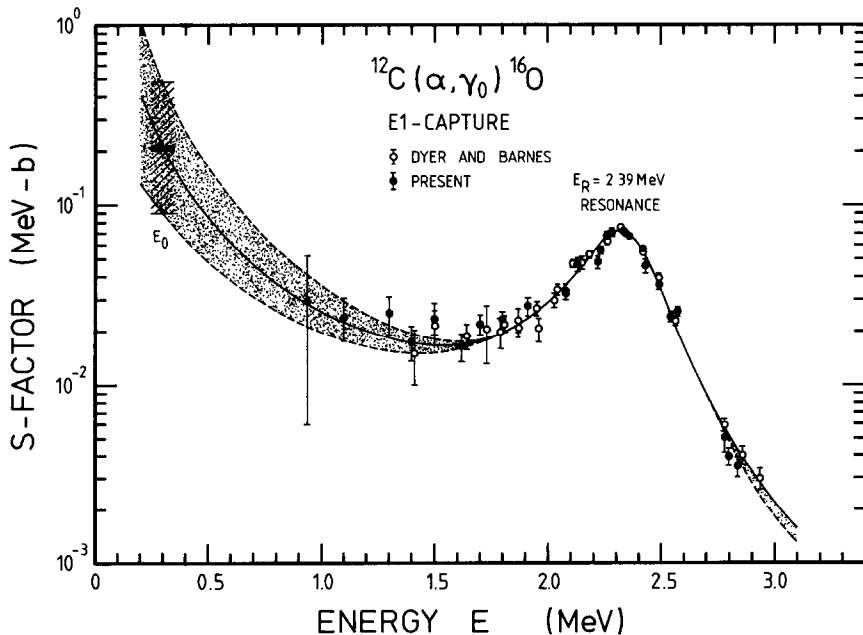
Fig. 4. The E1 cross-section data for $^{12}C(\alpha, \gamma_0)^{16}O$, as obtained at $\theta_\gamma = 90°$ in previous and present work and normalized to the same standard (sect. 3.1), are displayed in form of the astrophysical S-factor. The solid curve represents a three-level R-matrix fit to the combined data sets and the dotted area reflects the present uncertainty in the extrapolations to stellar energies at $E_0 = 0.3$ MeV (sect. 4.1).

TABLE 1

Summary of E1 capture data

E [a]) (MeV)	$S(E)$ [b]) (10^{-2} MeV · b)	E [a]) (MeV)	$S(E)$ [b]) (10^{-2} MeV · b)
0.94 ± 0.02	2.93 ± 2.31	2.26	6.69 ± 0.48 [c])
1.10 ± 0.02	2.39 ± 0.65	2.28	7.06 ± 0.40
1.30	2.49 ± 0.59	2.33	7.29 ± 0.48
1.40	1.74 ± 0.38	2.35	6.95 ± 0.30
1.50	2.36 ± 0.47	2.36	6.71 ± 0.29 [c])
1.62	1.63 ± 0.28	2.42	5.68 ± 0.28
1.70	2.18 ± 0.29	2.43	4.58 ± 0.37
1.80	2.32 ± 0.20	2.49	3.59 ± 0.22
1.91	2.73 ± 0.31	2.54	2.41 ± 0.15
2.08	3.35 ± 0.33	2.57	2.57 ± 0.14
2.13	4.68 ± 0.42	2.78	0.502 ± 0.082
2.22	4.80 ± 0.40	2.80	0.396 ± 0.042
2.23	5.57 ± 0.32	2.84	0.348 ± 0.044

[a]) Effective energy within the target (error = ±10 keV, except where quoted).

[b]) The errors assigned are predominantly statistical. An overall error of 6% has to be added from uncertainties in the standard cross section (sect. 3.1).

[c]) Obtained in the course of measurements of the absolute cross section (sect. 3.1).

data reported by Dyer and Barnes [5]), which have been scaled to the standard (sect. 3.1). Good agreement between both data sets is noted in the overlapping energy region (for extrapolation to stellar energies, see sect. 4.1).

3.3. ANGULAR DISTRIBUTIONS AND RATIO OF E1 AND E2 CAPTURE CROSS SECTIONS

Angular distributions were obtained with NaI(Tl) crystals (first experiment) at $E = 1.75$–2.84 MeV and with germanium detectors (second experiment) at $E = 1.71$–2.83 MeV. Results at representative energies are illustrated in fig. 5. The angular distributions, measured at the $J^\pi = 2^+$ resonance at $E_R = 2.68$ MeV (e.g., fig. 5c), have the familiar E2 pattern, while the distributions at other energies are asymmetric about 90°, clearly indicating the presence of both E1 and E2 amplitudes in the capture mechanism. Analyses of these distributions involve [5]) two parameters, the ratio of the capture cross sections σ_{E2}/σ_{E1} and the relative phase Φ between these multipole transitions:

$$W(\theta_\gamma) = 1 - Q_2 P_2(\theta_\gamma) + (\sigma_{E2}/\sigma_{E1})(1 + \tfrac{5}{7}Q_2 P_2(\theta_\gamma) - \tfrac{12}{7}Q_4 P_4(\theta_\gamma))$$

$$+ \tfrac{6}{5}(5\sigma_{E2}/\sigma_{E1})^{1/2} \cos \Phi(Q_1 P_1(\theta_\gamma) - Q_3 P_3(\theta_\gamma)) .$$

Here, the $P_k(\theta_\gamma)$ are the Legendre polynomials and the Q_k are the attenuation

TABLE 2

Summary of angular distribution results

E [a] (MeV)	σ_{E2}/σ_{E1} [b]	ϕ [b] (deg)	χ^2 [c]
	8 NaI(Tl) crystals		
1.75	0.21 ± 0.17	42 ± 42	2.1
1.91	0.28 ± 0.19	53 ± 27	0.5
2.00	0.41 ± 0.12	60 ± 10	0.9
2.09	0.18 ± 0.07	46 ± 8	1.8
2.16	0.16 ± 0.05	46 ± 6	1.3
2.24	0.19 ± 0.06	54 ± 7	1.3
2.31	0.12 ± 0.04	47 ± 10	1.4
2.38	0.15 ± 0.06	53 ± 9	1.1
2.45	0.21 ± 0.07	62 ± 9	1.4
2.53	0.38 ± 0.08	69 ± 5	2.4
2.63	0.41 ± 0.22	73 ± 14	0.6
2.84	1.10 ± 0.30	85 ± 12	0.8
	6 germanium detectors [d]		
1.71	0.31 ± 0.09	44 ± 10	2.1
1.80	0.16 ± 0.08	20 ± 20	0.8
1.83	0.07 ± 0.03	56 ± 8	2.2
1.92	0.05 ± 0.03	17 ± 17	2.9
1.98	0.10 ± 0.02	19 ± 19	6.2
2.02	0.13 ± 0.07	38 ± 14	1.9
2.06	0.08 ± 0.03	17 ± 17	1.7
2.12	0.14 ± 0.06	50 ± 11	2.5
2.17	0.05 ± 0.02	18 ± 18	4.1
2.25	0.03 ± 0.02	13 ± 13	5.3
2.26	0.05 ± 0.02	13 ± 13	3.4
2.30	0.04 ± 0.03	24 ± 24	1.8
2.36	0.05 ± 0.03	26 ± 26	3.4
2.40	0.04 ± 0.02	30 ± 30	0.04
2.45	0.16 ± 0.06	64 ± 7	0.7
2.49	0.09 ± 0.06	65 ± 11	1.0
2.54	0.12 ± 0.07	67 ± 11	1.4
2.61	0.28 ± 0.09	74 ± 8	1.3
2.83	0.32 ± 0.10	88 ± 7	1.7
	3 germanium detectors [e]		
0.94 ± 0.02	1.50 ± 0.60	69 ± 9	0.9
1.10 ± 0.02	0.56 ± 0.22	66 ± 11	0.02
1.30	0.46 ± 0.18	72 ± 11	0.03
1.40	0.25 ± 0.13	59 ± 5	2.1
1.50	0.40 ± 0.15	53 ± 12	0.02
1.62	0.08 ± 0.04	21 ± 21	2.1
1.70	0.40 ± 0.10	63 ± 8	0.1
1.80	0.18 ± 0.09	58 ± 8	0.9
1.91	0.11 ± 0.05	19 ± 19	3.1
2.08	0.05 ± 0.02	18 ± 18	0.6
2.13	0.08 ± 0.08	36 ± 20	0.06
2.22	0.22 ± 0.10	63 ± 5	0.01
2.23	0.11 ± 0.05	58 ± 7	0.3

TABLE 2—*contd.*

E [a]) (MeV)	σ_{E2}/σ_{E1} [b])	ϕ [b]) (deg)	χ^2 [c])
2.28	0.06 ± 0.02	13 ± 13	0.3
2.33	0.03 ± 0.02	16 ± 16	1.5
2.35	0.03 ± 0.02	30 ± 30	0.3
2.42	0.02 ± 0.01	15 ± 15	3.2
2.43	0.14 ± 0.07	58 ± 15	0.2
2.49	0.19 ± 0.06	75 ± 5	0.8
2.54	0.06 ± 0.04	22 ± 22	0.1
2.57	0.30 ± 0.08	82 ± 10	6.4
2.78	0.04 ± 0.03	34 ± 34	0.5
2.80	0.08 ± 0.08	89 ± 13	0.1
2.84	0.28 ± 0.10	87 ± 8	0.01

[a]) The values were determined from the incident beam energies corrected for target thickness effects (NaI(Tl) crystals: error = ±15 keV) or from the energies of the γ_0 ray centroids (germanium detectors: error = ±10 keV, except where quoted).
[b]) One standard deviation error.
[c]) Reduced χ^2 values for 5 degrees of freedom (8 NaI(Tl) crystals) and 3 degrees of freedom (6 germanium detectors). In the experiment using 3 germanium detectors the norm $\sigma_{E1}(E)$ was taken from the curve of fig. 4, thus resulting in 1 degree of freedom.
[d]) Preliminary results of these measurements have been reported previously [12]). Reanalyses of the data led to slightly different values reported here.
[e]) The errors quoted for the σ_{E2}/σ_{E1} ratios include the uncertainty in the $\sigma_{E1}(E)$ norm (dotted area in fig. 4).

coefficients calculated [15]) for the detector geometries. The resulting parameters describing the angular distributions are summarized in table 2.

Finally, the excitation functions obtained with 3 germanium detectors (third experiment) were analyzed using the above expression and the values for $\sigma_{E1}(E)$ from the solid curve in fig. 4. The results are given also in table 2. The ratios σ_{E2}/σ_{E1}, obtained within 100 keV energy intervals, have been averaged and the results are displayed in fig. 6 together with the data from previous work [5]). Similarly, the relative phase Φ is shown in fig. 7.

3.4. GAMMA-RAY DECAY OF THE 2.68 MeV RESONANCE

In the course of absolute cross section measurements using 6 germanium detectors (sect. 3.1), the γ-ray decay scheme of the $J^\pi = 2^+$, $E_R = 2.68$ MeV resonance was reinvestigated (fig. 3a). A new γ-ray branch, $R \to 7.12$ MeV, of $(4 \pm 2)\%$ was found.
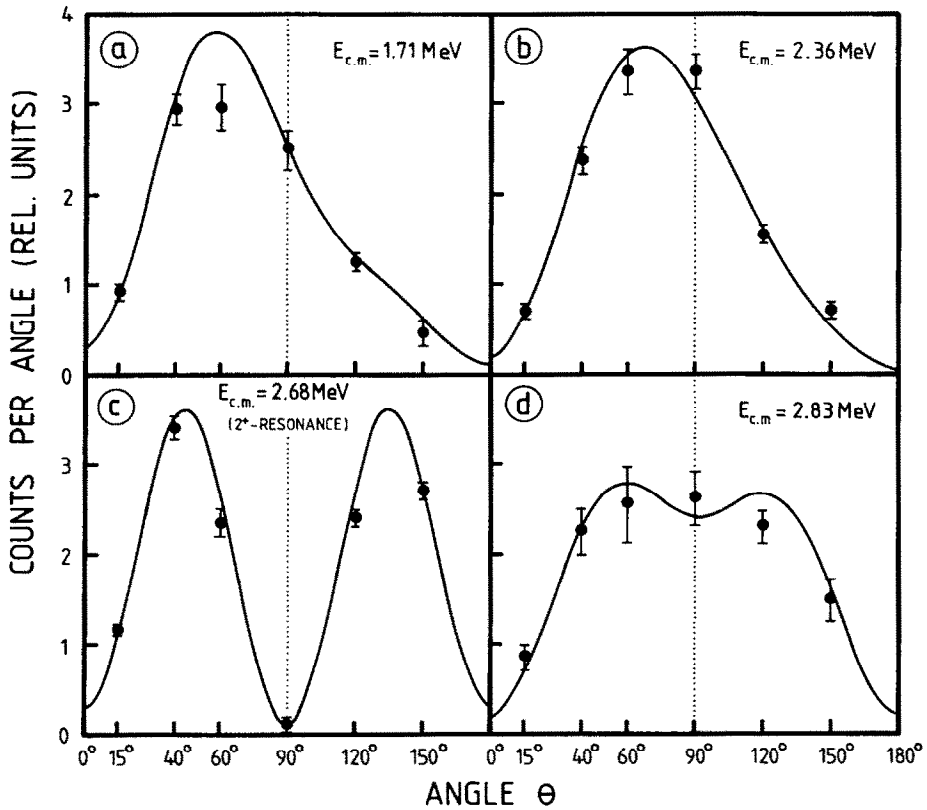
Fig. 5. Representative angular distributions of the ground-state transition in the reaction $^{12}C(\alpha, \gamma_0)^{16}O$. The data have been obtained with germanium detectors and implanted ^{12}C targets. The lines through the data points are the results of χ^2 fits that included E1–E2 interference effects.

The other $R \to 0$, $R \to 6.05$ and $R \to 6.92$ MeV decays proceed to (62 ± 3), (20 ± 3) and $(14 \pm 3)\%$, in good agreement with previous values [11]) of (61 ± 4), (18 ± 4) and $(21 \pm 4)\%$, respectively. The $R \to 6.92$ MeV γ-ray angular distribution is described by the coefficients $a_2 = -0.18 \pm 0.13$ and $a_4 = -0.28 \pm 0.19$ leading [15]) to a multipole mixing ratio of $\delta(E2/M1) = -0.5 \pm 0.1$. Using an observable γ-ray width [11]) of $\Gamma_\gamma^*(R \to 6.92) = 1.5 \pm 0.3$ meV (corrected [15]) for the new branches), the E2 strength of this transition is 0.7 ± 0.3 W.u. The available angular distribution data of the weak branch, $R \to 7.12$ MeV, did not allow a meaningful analysis, due to sizable non-resonant yield contributions (sect. 3.5).

3.5. EXCITATION FUNCTIONS OF CASCADE TRANSITIONS

With the use of $\gamma\gamma$-coincidences between NaI(Tl) crystals, Kettner et al. [6]) found cascade γ-ray transitions via the $(6.92 + 7.12)$ MeV excited states of ^{16}O (fig. 1). Due to the lack of good energy resolution, the individual contributions via these two
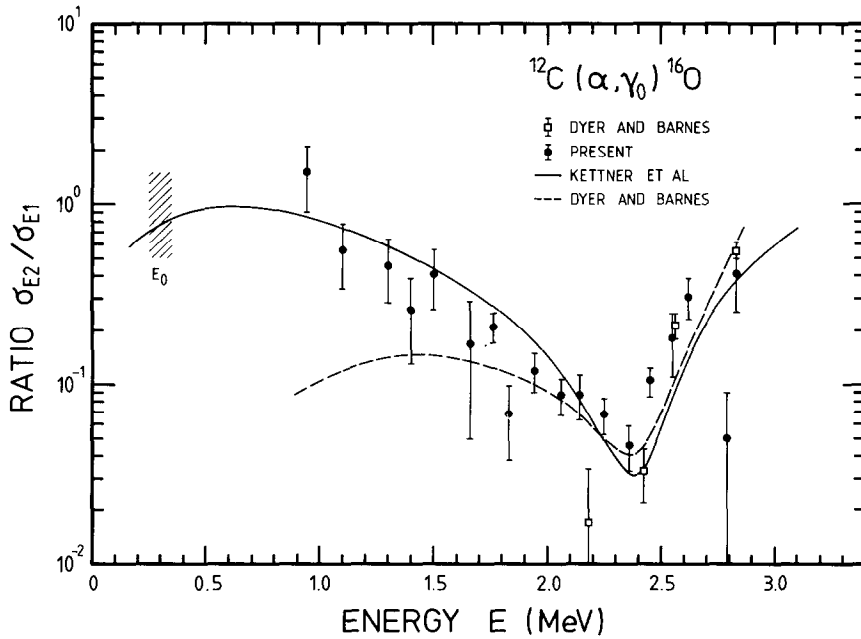
Fig. 6. Energy dependence of the ratio σ_{E2}/σ_{E1} obtained from the analysis of γ-ray angular distributions for $^{12}C(\alpha, \gamma_0)^{16}O$. Data over 100 keV energy intervals have been averaged. Also shown are the results reported by Dyer and Barnes [5]. The solid line is obtained from the E1 and E2 curves of fig. 14a of Kettner *et al.* [6] The model calculations of Dyer and Barnes [5] (dashed curve) included only the DC process (i.e., not the -245 keV subthreshold resonance).

states could not be resolved. In the analyses of these data it was asumed [6] that the observed yields arise predominantly from the cascade via the 6.92 MeV state.

The primary γ-ray transitions of these $\gamma\gamma$-cascades appear energetically in regions which are dominated by beam-induced γ-ray background (fig. 3b), and thus their detection – even when using germanium detectors – is hampered severely. However, the secondary γ-ray transitions, $6.92 \rightarrow 0$ and $7.12 \rightarrow 0$ MeV, could be observed (fig. 3b). Considerations of possible background reactions (target and ion beam contaminations) indicated that the existence of both secondary transitions alone could only be explained as arising from the $^{12}C(\alpha, \gamma)^{16}O$ reaction. The resulting excitation functions [15] (second and third experiment) are shown in fig. 8 and numerical values are given in table 3. The summed yields for both transitions are in good agreement with previous coincidence work using NaI(Tl) crystals [6], thus strengthening the above considerations. However, the new data reveal that both $\gamma\gamma$-cascades are resonant at the $E_R = 2.39$ MeV resonance ($J^\pi = 1^-$) with branches of (63 ± 6), (6 ± 6) and $(31 \pm 6)\%$ for the $R \rightarrow 0$ (0^+), $R \rightarrow 6.92$ (2^+) and $R \rightarrow 7.12$ (1^-) MeV transitions (sect. 4).

The deduced γ-ray width of $\Gamma_\gamma^*(R \rightarrow 6.92) = 1.4 \pm 1.4$ meV (an alternative approach in the analysis of the data yields a width of 2.2 ± 1.4 meV; sect. 4.3) leads to upper
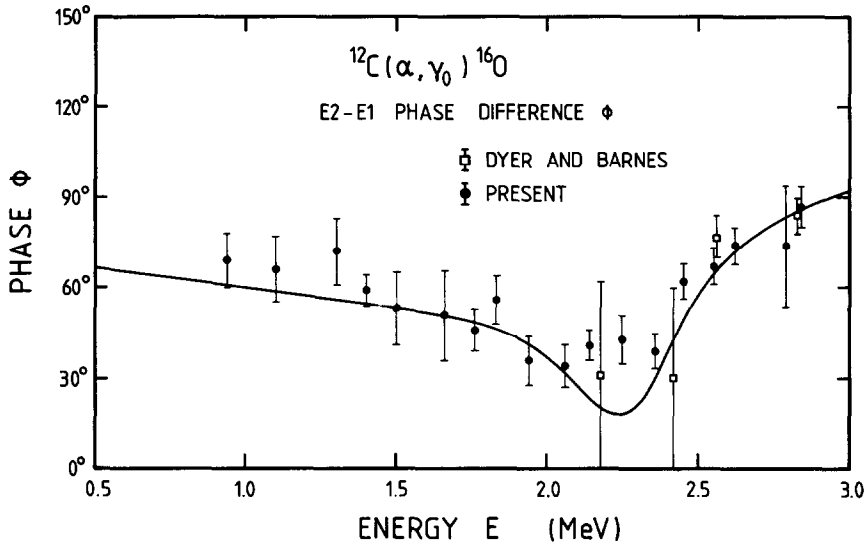
Fig. 7. Energy dependence of the E2-E1 phase difference ϕ obtained from the analysis of angular distributions for $^{12}C(\alpha, \gamma_0)^{16}O$. Data over 100 keV energy intervals have been averaged. Also shown are the results of Dyer and Barnes [5]. The solid curve is obtained from a simple model [5], in which the phase is described by the expression $\phi = \delta(l = 1) - \delta(l = 2) - \arctan \eta/2$, i.e., the difference between the experimental elastic scattering phase shifts and the Coulomb phase shifts for $l = 1$ and $l = 2$ (see also refs. [27,31]).

limits for the transition strengths of $E1 = (1.8 \pm 1.8) \times 10^{-4}$ W.u. and $M2 = 116 \pm 116$ W.u. From the recommended upper limit for isospin-retarded M2 transitions [23] (RUL = 0.1 W.u.), one concludes that the $R \rightarrow 6.92$ MeV transition must proceed nearly 100% via E1 radiation. The angular distributions for the $6.92 \rightarrow 0$ MeV secondary transition, calculated near $E_R = 2.39$ MeV for this E1 resonant transition and including the direct capture contributions E2 (s, d, g $\rightarrow$ 3d), are consistent with observation [15]. The observed distributions at $E \leqslant 2.1$ MeV are nearly isotropic and are consistent with the direct capture process as the major capture mechanism at these energies.

The angular distributions for the $7.12 \rightarrow 0$ MeV transition near the maximum of the $E_R = 2.39$ MeV resonance (fig. 8b) are described [15] by the coefficient $a_2 = 0.0 \pm 0.1$, leading to a multipole mixing ratio of $|\delta| \geqslant 1.4$ for the $R \rightarrow 7.12$ MeV primary transition. From a fit to the data (sect. 4.3) an observable γ-ray width of $\Gamma_\gamma^*(R \rightarrow 7.12) = 7.8 \pm 1.6$ meV is found. This width together with the mixing ratio lead to transition strengths of $M1 \leqslant 0.010$ W.u. and $E2 \geqslant 24$ W.u. The large E2 strength suggests a close relationship between the 7.12 and 9.55 MeV states. In comparison, the $R \rightarrow 0$ MeV transition is strongly retarded ($E1 = 4.1 \times 10^{-5}$ W.u.).

The above observations for the cascade transitions might represent interesting input parameters for improved microscopic-model calculations used in the analyses of the $^{12}C(\alpha, \gamma)^{16}O$ capture data [8-10]. For example, the sizable strength of $E2(6.92 \rightarrow 0) = 3.2$ W.u. (ref. [11]) indicates also a close relationship between the ground state
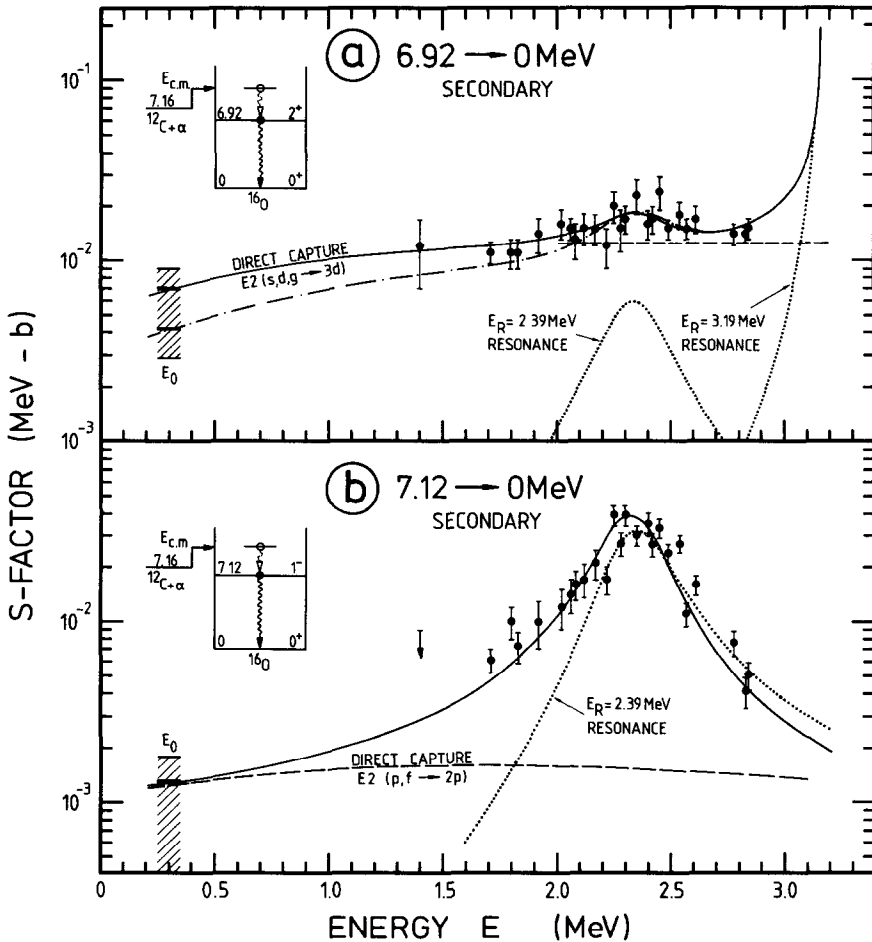
Fig. 8. *S*-factor data for the 6.92 → 0 and 7.12 → 0 MeV secondary transitions in $^{12}C(\alpha, \gamma)^{16}O$ are shown together with their interpretations (sect. 4.3). The direct capture curves represent the summed contributions from the various initial partial waves.

and the 6.92 MeV state and, thus, the ratio of E1 strengths for the $R \rightarrow 6.92$ and $R \rightarrow 0$ MeV transitions should reflect the ratio of α clustering in the final state wave functions, i.e., $\theta_\alpha^2(6.92)/\theta_\alpha^2(0) \approx E1(R \rightarrow 6.92)/E1(R \rightarrow 0) = 4.3 \pm 4.3$ (or 6.8 ± 4.3, sect. 4.3), if both final states are pure $T = 0$ states.

4. Discussion

In the interpretation of the experimental cross sections, it is necessary to consider contributions to the interaction matrix element both from the direct (extranuclear) capture amplitudes [24]) and from the resonant capture amplitudes [25]). The latter amplitudes include contributions from all bound and continuum states of ^{16}O.

TABLE 3

Excitation functions of cascade transitions

$E^{a)}$ (MeV)	S-factor $^{b)}$ $(10^{-2}$ MeV · b)	
	6.92 → 0 MeV	7.12 → 0 MeV
1.40	1.2 ± 0.5	≤0.9
1.71	1.10 ± 0.14	0.61 ± 0.09
1.80	1.1 ± 0.2	1.0 ± 0.2
1.83	1.1 ± 0.2	0.73 ± 0.14
1.92	1.4 ± 0.3	1.0 ± 0.3
2.02	1.6 ± 0.3	1.2 ± 0.3
2.06	1.5 ± 0.2	1.4 ± 0.3
2.08	1.3 ± 0.3	1.6 ± 0.3
2.12	1.5 ± 0.3	1.7 ± 0.3
2.17	1.5 ± 0.3	2.1 ± 0.4
2.22	1.2 ± 0.3	1.7 ± 0.3
2.25	2.0 ± 0.4	3.9 ± 0.5
2.28	1.5 ± 0.4	2.7 ± 0.4
2.30	1.7 ± 0.3	3.9 ± 0.5
2.35	2.3 ± 0.5	3.0 ± 0.4
2.40	1.6 ± 0.3	3.5 ± 0.5
2.42	1.7 ± 0.3	2.7 ± 0.4
2.45	2.4 ± 0.5	3.3 ± 0.4
2.49	1.5 ± 0.2	2.4 ± 0.3
2.54	1.8 ± 0.3	2.7 ± 0.3
2.57	1.5 ± 0.2	1.10 ± 0.16
2.61	1.7 ± 0.3	1.6 ± 0.2
2.78	1.4 ± 0.2	0.76 ± 0.12
2.83	1.40 ± 0.15	0.41 ± 0.08
2.84	1.5 ± 0.2	0.51 ± 0.09

$^{a)}$ See footnote $^{a)}$ of table 2.
$^{b)}$ One standard deviation error.

Although this division of the matrix element into two mechanisms is somewhat arbitrary, it is a useful division because the energy dependence is different for the two mechanisms and it is often possible to ignore one or the other mechanism over certain ranges of energy. It is also important to identify the dominant contributions to the cross section both in the region spanned by the measurements, and in the astrophysically interesting low-energy region ($E_0 = 0.3$ MeV).

4.1. THE E1 CAPTURE DATA

The E1 capture amplitudes from p-wave scattering states of $\alpha + {}^{12}C$ into the ^{16}O ground state can arise from the resonant capture mechanism through the $J^{\pi} = 1^-$ states in ^{16}O as well as the direct capture mechanism E1 (p → 3s). The single-level Breit–Wigner formula [25] (including the energy dependence of the partial and total widths and the level shift) was used [5,6] to estimate the resonant capture cross

sections. The calculations indicated that only the $J^\pi = 1^-$ states at $E_x = 7.12$ and 9.55 MeV (fig. 1) are of major importance at $E \leqslant 3.5$ MeV. The data shown in fig. 4 support qualitatively this expectation: the shape of the $E_R = 2.39$ MeV resonance does not reflect a normal Breit–Wigner form and requires constructive (destructive) interference effects at energies below (above) the resonance energy. It should be noted that the observation of the 7.12 MeV state contribution to the E1 capture data is possible only because of this interference between the two 1^- states.

To analyze quantitatively the E1 capture data, the many-level R-matrix formalism of nuclear reactions [25]) is used, which is in principle an exact theory as long as a complete set of states is used. In practice, however, only a severely restricted number of states can be handled, and ambiguities arise in the choice of the nuclear radius R_n and the boundary condition parameter B. Weisser *et al.* [26]) and Barker [27]) have used a three-level R-matrix formalism to parametrize the $\alpha + ^{12}C$ elastic scattering p-wave phase shifts and the $^{12}C(\alpha, \gamma_0)^{16}O$ E1 cross sections. They have demonstrated that the cross sections extrapolated to astrophysical energies are not sensitive to moderate variations of the nuclear radius, and are quite insensitive to the choice of B, even when only three states are included. Barker [27]) also showed analytically that different choices of B lead to the same predicted cross sections when appropriate changes are made in other parameters. The three levels included in these analyses are the 7.12 MeV state, the 9.55 MeV state, and a fictitious state at 20 MeV excitation energy, the low-energy wing of which is to represent any other 1^- background (such as the giant dipole resonance and/or the E1 (p $\to$ 3s) direct capture process) in the energy region of interest. Their expression [26,27]) for the E1 cross section is

$$\sigma_{E1} = \frac{3\pi}{k^2} \left| \sum_{\lambda, \lambda'=1}^{3} \Gamma_{\lambda\alpha}^{1/2} A_{\lambda\lambda'} \Gamma_{\lambda'\gamma}^{1/2} \right|^2,$$

where the level matrix $A_{\lambda\lambda'}$ is most conveniently defined by its inverse

$$(A^{-1})_{\lambda\lambda'} = (E_\lambda - E)\delta_{\lambda\lambda'} + \Delta_{\lambda\lambda'} - \tfrac{1}{2}i\Gamma_{\lambda\alpha}^{1/2}\Gamma_{\lambda'\alpha}^{1/2}$$

and k is the wave number in the entrance channel. The symbols $\Gamma_{\lambda\alpha}$, $\Gamma_{\lambda\gamma}$ and E_λ are the α-widths, the γ-widths and the eigen energies of the three levels, respectively. The level-shift matrix $\Delta_{\lambda\lambda'}$ is a function [26,27]) of the reduced α-particle widths,

$$\theta_{\lambda\alpha}^2 = \frac{\gamma_{\lambda\alpha}^2}{3\hbar^2/2\mu R_n^2} \quad \text{with } \Gamma_{\lambda\alpha} = 2P_\alpha \gamma_{\lambda\alpha}^2,$$

the boundary condition parameter B and the $l = 1$ shift function, S_α:

$$\Delta_{\lambda\lambda'} = -(S_\alpha - B)\gamma_{\lambda\alpha}\gamma_{\lambda'\alpha}.$$

The observable α-particle width $\Gamma_{\lambda\alpha}^*$ is connected with the formal width $\Gamma_{\lambda\alpha}$ via

the relation [25,26,27])

$$\Gamma^*_{\lambda\alpha} = \Gamma_{\lambda\alpha}(1 + \gamma^2_{\lambda\alpha}\, \mathrm{d}S_\alpha/\mathrm{d}E)^{-1} .$$

A similar relation is found for the γ-widths,

$$\Gamma^*_{\lambda\gamma} = \Gamma_{\lambda\gamma}(1 + \gamma^2_{\lambda\alpha}\, \mathrm{d}S_\alpha/\mathrm{d}E)^{-1}$$

and a reduced γ-width $\gamma^2_{\lambda\gamma}$ is defined [26]) as

$$\Gamma_{\lambda\gamma}(E) = \gamma^2_{\lambda\gamma}((7.16 + E)/(7.16 + E_\lambda))^3 .$$

Note that for a given state λ the above formulae for $\Gamma^*_{\lambda\alpha}$ and $\Gamma^*_{\lambda\gamma}$ are only valid [27]) for the choice $B = S_\alpha(E_\lambda)$.

In the present work we followed closely the procedures of Weisser *et al.* [26]). The radius, the boundary condition parameter and the eigen energy of the fictitious level were fixed [26]) at $R_n = 5.5$ fm, $B = -1.5$ and $E_3 = 13.0$ MeV. The B-value was chosen so that the level shift is equal to zero at the position of the $E_R = 2.39$ MeV resonance. Two parameters of the 7.12 MeV level, E_1 and $\gamma_{1\gamma}$, can be written in terms of the remaining parameters and the measured values [11]) of the excitation energy ($E_x = 7116.85 \pm 0.14$ keV) and of the observed γ-width of the state ($\Gamma^*_\gamma = 57 \pm 5$ meV). The parameters E_2, $\gamma_{2\alpha}$ and $\gamma_{3\alpha}$ were obtained [26]) by fitting the experimental p-wave phase shifts for $\alpha + {}^{12}C$ elastic scattering [22,28]) (table 4). The three remaining para-

TABLE 4

Best fit R-matrix parameters for $B = -1.5$
and $R_n = 5.5$ fm

Parameter	Value
E_1	-0.412 MeV
$\gamma_{1\alpha}$	0.59 MeV$^{1/2}$ [b])
$\gamma_{1\gamma}$	8.13 meV$^{1/2}$
E_2	2.39 MeV [a])
$\gamma_{2\alpha}$	0.774 MeV$^{1/2}$ [a])
$\gamma_{2\gamma}$	-4.96 meV$^{1/2}$ [c])
E_3	13.0 MeV [a])
$\gamma_{3\alpha}$	1.80 MeV$^{1/2}$ [a])
$\gamma_{3\gamma}$	15.6 meV$^{1/2}$

[a]) From Weisser *et al.* [26]).

[b]) Corresponding to a reduced α-particle width of $\theta^2_\alpha(7.12) = 0.11$ for a boundary parameter B equal to the shift factor S_α at the 7.12 MeV level [26]).

[c]) Corresponding to a formal γ-width of $\Gamma_\gamma = 24.6 \pm 1.8$ meV and an observable γ-width of $\Gamma^*_\gamma = 15.6 \pm 1.2$ meV.

meters $\gamma_{1\alpha}$, $\gamma_{2\gamma}$ and $\gamma_{3\gamma}$ were determined [15]) by fitting the $^{12}C(\alpha, \gamma_0)^{16}O$ E1 cross sections. Fits were made to the data of Dyer and Barnes [5]) and to the present data leading to identical curves to within 10%. The final parameters obtained from a fit to the combined data sets (table 4) were used to extrapolate the $S(E)$-factor curve (solid curve in fig. 4, $\chi^2 = 2.0$) to stellar energies: $S_{E1}(E_0 = 0.3$ MeV$) = 0.20$ (+0.28, −0.18) MeV · b. The quoted error was determined by observing the range of variations of $S_{E1}(E_0)$ over a contour of χ^2 values corresponding to one standard deviation error (minimum χ^2 plus number of degrees of freedom), which was traced out as a function of the parameters varied in the fit to the combined E1 capture data. The largest contributions to the error arise from uncertainties in the reduced α-particle width for the 7.12 MeV level and the γ-ray width of the fictitious background level. The variation in $S_{E1}(E_0)$ corresponds, within the three-level R-matrix fit, to a range of values $\theta_\alpha^2(7.12) = 0.01$ to 0.26. Note that the observable reduced width $\theta_\alpha^2(7.12)$ is not equal to the formal width $\theta_{1\alpha}^2$ but depends on the boundary parameter B (footnote [b]) of table 4). Analysis of the cascade transition via the 7.12 MeV level reveals (sect. 4.3) values of $\theta_\alpha^2(7.12) = 0.05$ to 0.48, leading to a concordant range of $\theta_\alpha^2(7.12) = 0.05$ to 0.26 and to $S_{E1}(E_0) = 0.20$ (+0.27, −0.11) MeV · b. The resulting range of S-factor curves are presented by the dotted area in fig. 4.

Barker [27]) carried out a three-level R-matrix fit to the data of Jaszczak et al. [4]) resulting in $S_{E1}(E_0) = 0.15$ (+0.18, −0.06) MeV · b, and a fit to the original data of Dyer and Barnes [5]) led [31]) to $S_{E1}(E_0) = 0.16$ (+0.15, −0.06) MeV · b. Other three-level R-matrix fits to the original data of Dyer and Barnes [5]) yielded $S_{E1}(E_0) = 0.14$ (+0.14, −0.12) MeV · b [ref. [5])] and 0.17 MeV · b [ref. [26])]. Kettner et al. [6]) reported from a Breit–Wigner analysis of their original angle-integrated data a value of $S_{E1}(E_0) = 0.25$ MeV · b. Recent hybrid R-matrix parametrizations [9]) of the original data of Dyer and Barnes [5]) and of Kettner et al. [6]) led* to values of $S_{E1}(E_0) = 0.16$ (or 0.17) MeV · b and 0.28 (or 0.29) MeV · b, respectively. Finally, in the work of Descouvement et al. [8]) a value of 0.30 MeV · b was reported. These values are in fair agreement with the results from the present analyses, although an even better agreement might be expected to result if the analyses of the various data would have used the same standard for the absolute cross sections (sect. 3.1).

It is seen that the three-level R-matrix fits to the $^{12}C(\alpha, \gamma_0)^{16}O$ E1 capture data alone give $S(E_0)$ values with rather large uncertainties. As pointed out above, the reason for these uncertainties is due to the fact that the γ-ray width of the fictitious background level is free to vary in the three-level R-matrix parametrization. Since the effect of varying $\gamma_{3\gamma}$ is similar [5]) to the effect of varying $\theta_\alpha^2(7.12)$, both of these parameters must be assigned rather large errors. The $S(E_0)$ factor, which is more strongly dependent on $\theta_\alpha^2(7.12)$, becomes uncertain by a correspondingly large amount. To reduce the error in $S(E_0)$, Koonin et al. [7]) suggested the hybrid R-matrix model, in which the influence of the background strength at $E \leqslant 3$ MeV is derived from an $\alpha + ^{12}C$ optical potential rather from a fictitious background level, i.e., the

* The $\gamma_{i\alpha}$ values of the bound states reported in ref. 9 should be multiplied by a factor of 20.

γ-ray width of the background level is implicitly included in the model. Thus, the optical potential is the basic ingredient in the hybrid R-matrix model [7]).

The main idea of the hybrid R-matrix model is to split the R-functions into two parts

$$R_{\alpha\alpha} = R_{\alpha\alpha}(0) + R_{\alpha\alpha}(7.12),$$

$$R_{\alpha\gamma} = R_{\alpha\gamma}(0) + R_{\alpha\gamma}(7.12),$$

where the bracket (7.12) refers to the 7.12 MeV level and the bracket (0) to the broad level at $E_x = 9.55$ MeV (fig. 1) as well as to high-lying levels and direct processes. In this model, the quantities with bracket (0) are calculated within a potential model, in which the nucleus-nucleus potential is fitted to reproduce the experimental $\alpha + {}^{12}C$ p-wave phase shifts at $E \leq 3$ MeV. The free parameters are $\theta_\alpha^2(7.12)$ and the dipole strength d of the $\alpha + {}^{12}C$ scattering states, which are determined by fitting the ${}^{12}C(\alpha, \gamma_0){}^{16}O$ E1 capture data. Similar to the procedures of Koonin et al. [7]), we adopted – in a first approach – for the $\alpha + {}^{12}C$ optical potential a Woods–Saxon potential ($W_0 = -45.55$ MeV, $R_n = 3.55$ fm, $a = 0.6$ fm). In the second approach, we parametrized the optical potential by the gaussian form factor as described by Langanke and Koonin [9]) ($V_0 = -131.65$ MeV, $a = 2.6$ fm). Both potentials give equivalently good fits to the experimental p-wave phase shifts at $E \leq 3$ MeV. The relative wave function of the ${}^{16}O$ ground state, needed in the calculation of the $R_{\alpha\gamma}(0)$ function, was obtained as described in sect. 4.2.

The best fit to the combined E1 capture data (fig. 4) using the Woods–Saxon potential ($\chi^2 = 1.5$) was obtained for $d = 9.5$ and $\gamma_{1\alpha} = -0.37$ MeV$^{1/2}$, or equivalently $\theta_\alpha^2(7.12) = 0.04$ (+0.05, −0.03), leading to $S_{E1}(E_0) = 0.09$ (+0.10, −0.06) MeV · b. The quoted error for $S_{E1}(E_0)$ was obtained as described above (i.e., by variation of the fitted parameters d and $\gamma_{1\alpha}$). The gaussian potential resulted in $\chi^2 = 2.0$, $d = 4.2$, $\gamma_{1\alpha} = -0.56$ MeV$^{1/2}$ ($\theta_\alpha^2(7.12) = 0.07$ (+0.05, −0.04)) and $S_{E1}(E_0) = 0.14$ (+0.12, −0.08) MeV · b. These results are consistent with previous hybrid R-matrix parametrizations of the original data of Dyer and Barnes [5]): Woods–Saxon potential with $S_{E1}(E_0) = 0.08$ (+0.05, −0.04) MeV · b [ref. [7]] and gaussian potential with $S_{E1}(E_0) \approx 0.16$ MeV · [ref. [9]].

These studies show that the two optical potentials lead to different results for $S_{E1}(E_0)$, although both potentials are approximately phase-equivalent at $E \leq 3$ MeV. The principal reason for this difference appears to be that the two potentials treat the optical-model background differently and thus come to different values for $\theta_\alpha^2(7.12)$. With improved data for the p-wave phase shifts at $E \geq 3$ MeV, it appears possible to distinguish between the two potentials and thus to improve the hybrid R-matrix parametrizations. Such improved data might also help to clarify the systematically lower $S_{E1}(E_0)$ values compared to those obtained from the three-level R-matrix fits.

4.2. THE E2 CAPTURE DATA

Using the solid curve in fig. 4 for the E1 capture cross section (or equivalently for the $S_{E1}(E)$ factor) and the ratios σ_{E2}/σ_{E1} of fig. 6, the resulting E2 capture cross sections are shown in fig. 9 in form of the S-factor. The errors shown include the uncertainties in the $\sigma_{E1}(E)$ norm (dotted area in fig. 4). Similarly, subtracting the E1 cross sections (solid curve in fig. 4) from the total capture cross sections reported by Kettner et al.[6] (normalized to the standard, sect. 3.1), these resulting E2 capture data (averaged over 100 keV energy intervals) are also displayed in fig. 9. The E2 capture data show qualitatively an increase in the S-factor with decreasing energy, indicating a nonnegligible E2 contribution to the total S-factor at stellar energies.

Calculations[6] showed that the E2 resonant capture arises predominantly from the $J^{\pi} = 2^{+}$ states at $E_{x} = 6.92$ and 9.85 MeV (fig. 1) in the energy region below $E = 3.5$ MeV. The narrow 9.85 MeV state[11] ($\Gamma = 0.62$ keV) can influence the data[10] only at energies near the resonance energy ($E_{R} = 2.68$ MeV). Another E2 capture amplitude can arise from the E2 (d → 3s) direct capture process, where the absolute
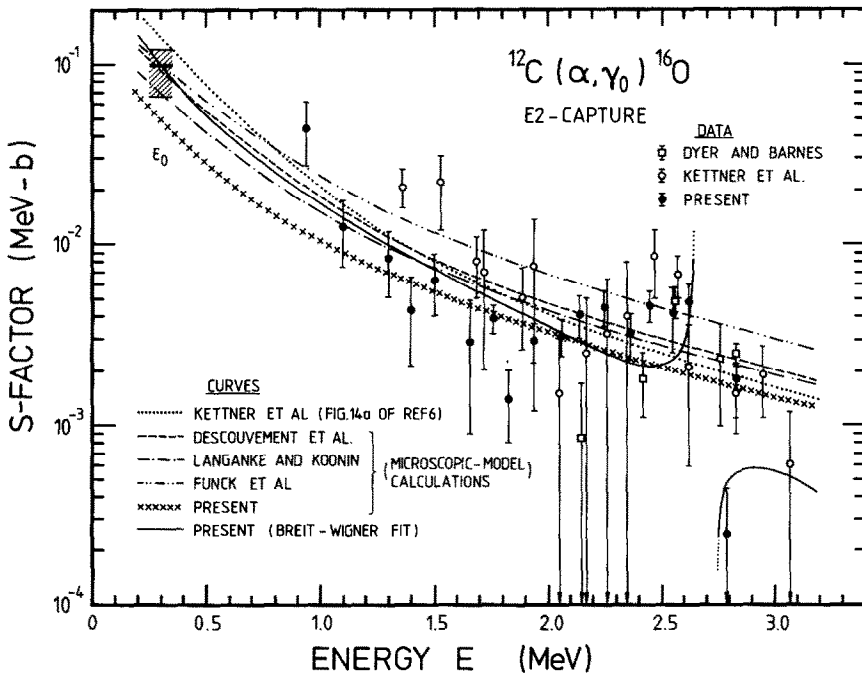

Fig. 9. S-factor data for the E2-capture amplitude in $^{12}C(\alpha, \gamma_{0})^{16}O$ as determined from the ratios σ_{E2}/σ_{E1} of fig. 6 and the solid curve for E1 capture in fig. 4. Also shown are data deduced from the angle-integrated cross sections reported by Kettner et al.[6] and the solid curve in fig. 4. The solid line through the data points represents a Breit-Wigner fit including interference effects with the narrow $E_{R} = 2.68$ MeV resonance. The dotted curve is extracted from fig. 14a of ref.[6]. The other curves are predictions of various microscopic-model calculations[8-10]. The microscopic-model curve labelled present is discussed in the text (sect. 4.2).

scale depends on the reduced α-particle width of the ground state, θ_α^2(g.s.). In addition, interference effects between the high-energy wing of the $E_R = -245$ keV subthreshold resonance and the direct capture process must be taken into account.

Similar to previous analyses [6]), the E2 capture data (fig. 9) were fitted with the expression

$$S_{E2}(E) = S_{R1}(E) + \frac{1}{\Delta} \int_{E-\Delta}^{E} S_{R2}(E')\, dE' + S_{DC}(E)$$

$$+ 2S_{R1}^{1/2}(E) \frac{1}{\Delta} \int_{E-\Delta}^{E} S_{R2}^{1/2}(E') \cos \phi_1\, dE'$$

$$+ 2(S_{R1}(E)S_{DC}(E))^{1/2} \cos \phi_2 + 2S_{DC}^{1/2}(E) \frac{1}{\Delta} \int_{E-\Delta}^{E} S_{R2}^{1/2}(E') \cos \phi_3\, dE',$$

where the phase differences $\phi_i(E)$ were determined as described previously [6]). The $S_{R2}(E)$ factor for the narrow resonance at $E_R = 2.68$ MeV as well as the associated inteference terms have been integrated over the target thickness of $\Delta = 80$ keV. The free parameters in this "Breit–Wigner plus direct capture" fit [15]) to the capture data were θ_α^2(g.s.) and θ_α^2(6.92), the respective values of which were found to be 0.012 ± 0.012 and 0.07 to 0.72 from the fit to the combined data (fig. 9). Concordance with the analysis of the data for the cascade transitions via the 6.92 MeV state (sect. 4.3) restricts θ_α^2(6.92) $= 0.39 \pm 0.20$. With the value of 0.39 the solid curve in fig. 9 was calculated, and the range of the θ_α^2(6.92) values leads to $S_{E2}(E_0) = 0.096$ (+0.024, −0.030) MeV · b. Analysis of the angle-integrated data of Kettner et al. [6]) led to the dotted curve shown in fig. 9 with $S_{E2}(E_0) = 0.14$ MeV · b.

Various microscopic-model calculations have been carried out [8-10]) leading to $S_{E2}(E_0) = 0.07$ to 0.10 MeV · b (fig. 9). In particular, the coupled-channel approach of Funck et al. [10]) showed that the $S_{E2}(E)$ factor at $E \leqslant 2.2$ MeV is dominated by the high-energy wing of the 6.92 MeV subthreshold state and its inteference with a non-resonant background contribution, a conclusion similar to that reached by Kettner et al. [6]). This scenario is well described by the microscopic-potential model [9]), which is based on the fact that all states relevant to $S_{E2}(E_0)$ (i.e., the ground state, the 6.92 MeV state and the $\alpha + {}^{12}$C d-wave scattering states) can be described [9]) by antisymmetrized $\alpha + {}^{12}$C many-body cluster wave functions. The relative motion of the many-body states is derived from $\alpha + {}^{12}$C potentials, which in turn are fitted to reproduce relevant experimental data. We have performed a microscopic potential model calculation requiring that the $\alpha + {}^{12}$C s-wave potential (from which we derived the ^{16}O ground state) and the d-wave potential (from which we deduced the 6.92 MeV bound state and the d-wave scattering states) fulfill the following conditions:

(i) Reproduction of the binding energies of the ground state and 6.92 MeV state.
(ii) Reproduction of the rms-radius of the ^{16}O ground state [11]) ($\langle r^2 \rangle^{1/2} = 2.71$ fm).

(iii) The appropriate number of radial nodes ($n = 2$ for both bound states), to fulfill the requirements of the Pauli principle in the relative motion of the many-body states.

(iv) The lifetime of the 6.92 MeV state for γ-decay to the ground state ($\tau = 6.6 \pm 0.4$ fs, ref. [11])), where this transition is calculated using the bound states of the $\alpha + ^{12}C$ potentials.

Furthermore, we required the 6.92 MeV state to have a quadrupole moment of $Q = -16.5\ e \cdot \text{fm}^2$, which is derived from the $B(E2)$ strength of the $6.92 \rightarrow 6.05$ MeV transition. Here, we assumed that both states belong to an $\alpha + ^{12}C$ rotational band with a constant intrinsic quadrupole moment. Such an interpretation might be justified due to the studies of Baldock *et al.* [33]). This requirement is different to the approach in ref. [9]), where the potentials were constrained to the E2 strength of the $10.36 \rightarrow 6.92$ MeV transition. This latter strength is, however, noticeably larger than expected from the simple $\alpha + ^{12}C$ rotational band interpretation [33]).

The above requirements were fulfilled by adopting the Coulomb potential of ref. [9]) and a gaussian form factor for the nucleus–nucleus potentials with the parameters $V_0 = -110.83$ MeV, $a = 2.29$ fm for the potential in the $l = 0$ partial wave, and the parameters $V_0 = -113.05$ MeV, $a = 2.75$ fm for the potential in the $\alpha + ^{12}C$ d-wave. Using these potentials to derive the relative wave functions of the $\alpha + ^{12}C$ cluster states, we have calculated $\sigma_{E2}(E)$ for $^{12}C(\alpha, \gamma_0)^{16}O$ involving these many-body states. To calculate the matrix elements of the many-body quadrupole operator, we used the technique described previously [9]). The results (crossed curve in fig. 9) lead to $S_{E2}(E_0) = 0.05$ MeV $\cdot$ b, which is somewhat smaller than the values deduced from other microscopic studies (fig. 9). Note that the present microscopic potential model prediction agrees fairly well with the results obtained in the best Breit–Wigner fit to the E2 data alone. Similarly as in the Breit–Wigner fit, the present potential parametrization underestimates the direct capture part of the cascade transition via the 6.92 MeV state (fig. 8 and sect. 4.3), if this transition is calculated by adopting the bound state of the $l = 2$ potential as the final state and by deriving the $l = 0, 2$, and 4 scattering states from the $\alpha + ^{12}C$ d-wave potential where the latter is assumed to be l-independent. This underestimation might be interpreted as an indication that the value for $\theta_\alpha^2(6.92)$ involved in the potential model is too small. It can be corrected by adjusting the direct capture cross sections to those results obtained within the best fit for the cascade transition (sect. 4.3). In turn, this adjustment leads to a corrected value of $S_{E2}(E_0) = 0.080 \pm 0.025$ MeV $\cdot$ b, where the error is obtained from the adjustment to the direct capture contributions of fits to the cascade transition within one standard deviation. This result agrees well with the microscopic model predictions of refs. [8-10]).

It should be noted that the above calculations require d-wave phase shifts, which are not inconsistent with available experimental data [22]). However, the presentation of these data (fig. 13 of ref. [22])) does not allow a more sensitive test of the model calculations. Thus, improved data on d-wave phase shifts are desirable.

4.3. THE CASCADE TRANSITIONS

The excitation function for the capture process via the $E_x(J^\pi) = 6.92\ (2^+)$ MeV state (fig. 8a) can satisfactorily be explained by the incoherent superposition of the E1 contribution from the $E_R = 2.39$ MeV resonance (dotted curve in fig. 8a) and the E2 (s, d, g→3d) direct capture contribution (dashed curve in fig. 8a). The data at the highest energies can also have contributions from the $J^\pi = 4^+$, $E_R = 3.19$ MeV resonance amplitude (fig. 8a), in particular via interference effects with the E2 (g→ 3d) direct capture component. In comparison, the narrow resonance at $E_R = 2.68$ MeV (fig. 1) is too weak to influence significantly the data via interference effects. With the known resonance parameters of $E_R(\Gamma^*) = 2.39\ (0.384)$ MeV (sect. 4.1) and $E_R(\Gamma^*) = 3.19\ (0.027)$ MeV [ref. [11]], the free parameters were the γ-ray width of the $E_R = 2.39$ MeV resonance and $\theta_\alpha^2(6.92)$. The fit to the data (solid curve in fig. 8a, $\chi^2 = 0.7$) leads to an observable γ-width of $\Gamma_\gamma^* = 1.4 \pm 1.4$ meV, $\theta_\alpha^2(6.92) = 0.46 \pm 0.13$ and $S_{6.92}(E_0) = (7 \pm 2) \times 10^{-3}$ MeV · b (statistical errors only). The observed angular distributions for the 6.92→0 MeV secondary transition (section 3.5) are consistent with the above analysis.

In an alternative approach, the energy dependence of the E1 portion of the cross section via the 6.92 MeV state was assumed to be the same as that of the E1 groundstate cross section, except for the phase space factor E_γ^3. The latter cross section was obtained from the hybrid R-matrix parametrization of the γ_0 ray data (fig. 4 and sect. 4.1). The best fit to the data (dash-dot curve in fig. 8a, $\chi^2 = 0.7$) leads to $\Gamma_\gamma^* = 2.2 \pm 1.4$ meV, $\theta_\alpha^2(6.92) = 0.28 \pm 0.09$ and $S_{6.92}(E_0) = (4.2 \pm 1.3) \times 10^{-3}$ MeV · b. Both approaches together allow for values of $\theta_\alpha^2(6.92) = 0.39 \pm 0.20$ and $S_{6.92}(E_0) = (6 \pm 3) \times 10^{-3}$ MeV · b. Improved angular distribution data for this $\gamma\gamma$-cascade would allow to distinguish between these two approaches as well as to provide better information for $\theta_\alpha^2(6.92)$. Note also that the above assumption requires the existence of a 2.2×10^{-3}% branching ratio for the 7.12→6.92 MeV γ-ray decay.

The secondary transition of the $\gamma\gamma$-cascade via the 7.12 (1^-) MeV state exhibits a pronounced resonance behavior near $E_R = 2.39$ MeV (fig. 8b). However, using the known resonance parameters E_R and Γ^* (see above) in combination with the one-level R-matrix formula, the data cannot be explained alone by this resonance (dotted curve in fig. 8b) and indicate the presence of an interfering amplitude. Since the R→7.12 MeV transition proceeds predominantly via E2 multipole radiation (sect. 3.5) and since its excitation function is observed here via the 7.12→0 MeV secondary transition, the interfering amplitude must also be characterized by E2 radiation arising from p-waves in the $\alpha + ^{12}C$ channel. Such an amplitude can originate, e.g., from the direct capture process E2 (p→2p) into the 7.12 MeV state, leading to a nearly energy-independent $S(E)$-factor curve (dashed curve in fig. 8b, where a 30% E2 (f→2p) component is also included which is added incoherently to the $S(E)$-factor). The absolute scale of this direct capture curve depends on

$\theta_\alpha^2(7.12)$. In the analysis [15]), the experimental p-wave phase shifts [22]) were used. The best fit to the data (solid curve in fig. 8b, $\chi^2 = 3.0$) was obtained for an observable γ-width of $\Gamma_\gamma^*(R \to 7.12) = 7.8 \pm 1.6$ meV and $\theta_\alpha^2(7.12) = 0.20$ (+0.28, −0.15) (statistical errors only), leading to $S_{7.12}(E_0) = (1.3 \, (+0.5, -1.0)) \times 10^{-3}$ MeV · b.

5. Summary

The individual contributions from various capture transitions in $^{12}C(\alpha, \gamma)^{16}O$ to the total $S(E_0)$ factor are summarized in table 5. It can be seen from this table that $S(E_0)$ is about a factor 3 to 4 higher than the previously recommended value [1,7,30]) of $S(E_0) = 0.08$ MeV · b. Based on the data (E1) of Dyer and Barnes [5]), the preliminary experimental data (E1 and E2) from the present work and theoretical analyses carried out at Caltech and Münster, Caughlan et al. [34]) found $S(E_0) = 0.24$ MeV · b. This recommended value represents a reasonable evaluation and is not in contradiction with the final results of the present work ($S(E_0) = 0.22$ and 0.32 MeV · b). However, the errors associated with the major contributions are still substantial and require further measurements for their reductions. The problems associated with the various contributions as well as possible improvements are discussed in what follows.

As discussed in sect. 4.1, the two methods of parametrizing the E1 capture data for the groundstate transition give different "best-fit" results. In order to understand this feature, improved p-wave phase shifts of the $\alpha + {}^{12}C$ scattering states at $E \geqslant 3$ MeV are needed. Having such data available and also extending the E1 capture cross section measurements to significant higher energies, far above the range of

TABLE 5

Contributions to the $S(E_0)$ factor from various transitions

Final state (MeV)	J^π	θ_α^2		Radiation	$S(E_0)$ (MeV · b)	
		present	α-transfer [a])		TLRM [b])	HRM [c])
0	0^+	0.012 ± 0.012	0.070	E1	0.20	0.12
				E2	0.096	0.080
6.05	0^+		0.44	E2	0.013 [d])	
6.13	3^-		0.09	E2	2.9×10^{-4} [e])	
6.92	2^+	0.39 ± 0.20	0.39	E2	7.0×10^{-3}	4.2×10^{-3}
7.12	1^-	0.15 ± 0.10	0.16	E2	1.3×10^{-3}	
SUM					0.318	0.219

[a]) From ref. [29]), normalized to $\theta_\alpha^2(6.93) = 0.39$.
[b]) Three-level R-matrix fits (for uncertainties, see sect. 4).
[c]) Hybrid R-matrix fits (for uncertainties, see sect. 4).
[d]) Assuming a direct capture process E2 (d → 4s) with θ_α^2 (6.05) = 0.44.
[e]) Assuming a direct capture process E2 (p, f, h → 1f) with $\theta_\alpha^2(6.13) = 0.09$.

the present experiment, would reduce significantly the present errors for $S_{E1}(E_0)$ arrived at in both methods. Due to the low capture cross sections and the existence of strong and broad resonances in the $^{13}C(\alpha, n)^{16}O$ background reaction, this aim represents an enormous challenge to the experimentalist.

The data for the cascade transitions via the 7.12 MeV level (fig. 8b) provided additional information for $\theta^2_\alpha(7.12)$, which was used in the present work to restrict the range of possible $S_{E1}(E_0)$ values (sect. 4.1). Improved data for these transitions also can help to reduce further the uncertainties in $\theta^2_\alpha(7.12)$ and thus in $S_{E1}(E_0)$.

Predictions of microscopic-model calculations as well as fits to available experimental data (fig. 9 and ref. [6])) reveal that the E2 capture amplitude in $^{12}C(\alpha, \gamma_0)^{16}O$ at stellar energies is substantial. The extrapolated values are in the range $S_{E2}(E_0) =$ 0.06 to 0.14 MeV · b (sect. 4.2). The most critical parameter is $\theta^2_\alpha(6.92)$, the uncertainty of which could possibly be reduced by improved data for the cascade transitions via the 6.92 MeV state (fig. 8a) as well as improved data for α-transfer reactions (ref. [29]) and references therein) and for d-wave phase shifts in $\alpha + ^{12}C$ elastic scattering [32]).

The E2 transitions into the 0, 6.92 and 7.12 MeV states all have direct capture contributions revealing reduced α-particle widths of $\theta^2_\alpha = 0.012$, 0.39 and 0.15, respectively. The analysis of α-transfer data [29]) leads to relative θ^2_α values (table 5), which are in fair agreement with the above results. Using these reported values (normalized to $\theta^2_\alpha(6.92) = 0.39$), the E2 direct capture cross sections into the 6.05 and 6.13 MeV states have been calculated [15]). The results (table 5) show that, in spite of their small transition energy available, the sum of all cascade transitions make a non-negligible contribution of about 7 to 10% to the total $S(E_0)$ factor, where the largest contribution arises from the DC → 6.05 MeV process. Clearly, an experimental verification of these calculations is needed.

To summarize, both the E1 and E2 amplitudes from the resonant and direct capture processes are important both in the measured energy region and at astrophysical energies. The largest contribution to the total $S(E_0)$ factor arises from capture into the ground state, but capture into excited states is not completely negligible. A reduction in the present uncertainty of $S(E_0)$ has to await the results of present and future experiments, such as the experiments carried out presently at Caltech [35]) using the noval technique of γ-^{16}O recoil coincidences.

The significant increase of the $^{12}C(\alpha, \gamma)^{16}O$ reaction rate has stimulated several investigations (e.g., refs. [2,3])). It was found for a 25 solar mass model star that an increased $^{12}C(\alpha, \gamma)^{16}O$ rate increases the oxygen and its subsequent reaction products and lowers the carbon and its subsequent reaction products, resulting in an abundance distribution more consistent with solar abundances. Even more subtle, however, is its effect on the structure of presupernova models [3]). These models, with an increased $^{12}C(\alpha, \gamma)^{16}O$ rate, produce larger iron cores and are also affected both in the explosion mechanism and the mass range of compact remnants. It has also been found that the higher rate affects the evolution of higher mass stars (up to 100 solar

masses). Thus, it is both surprising and exciting[3]) that a single nuclear reaction cross section can so radically affect the views of stellar evolution and nucleosynthesis.

References

1) W.A. Fowler, Rev. Mod. Phys. **56** (1984) 149
2) F.K. Thielemann and W.D. Arnett, Nucleosynthesis – challenges and new developments, ed. W.D. Arnett and J.W. Truran (University of Chicago Press, 1985) p. 151
3) S.E. Woosley, Accelerated radioactive beams, ed. L. Buchmann and J.M. d'Auria (TRIUMF TRI-1, 1985) p. 4
4) R.J. Jaszczak, J.H. Gibbons and R.L. Macklin, Phys. Rev. **C2** (1970) 63 and 2452
5) P. Dyer and C.A. Barnes, Nucl. Phys. **A233** (1974) 495
6) K.U. Kettner, H.W. Becker, L. Buchmann, J. Görres, H. Kräwinkel, C. Rolfs, P. Schmalbrock, H.P. Trautvetter and A. Vlieks, Z. Phys. **A308** (1982) 73
7) S.E. Koonin, T.A. Tombrello and G. Fox, Nucl. Phys. **A220** (1974) 221
8) P. Descouvement, D. Baye and P.H. Heenen, Nucl. Phys. **A430** (1984) 426
9) K. Langanke and S.E. Koonin, Nucl. Phys. **A410** (1983) 334 and **A439** (1985) 384
10) C. Funck, K. Langanke and A. Weiguny, Phys. Lett. **152** (1985) 11
11) F. Ajzenberg-Selove, Nucl. Phys. **A375** (1982) 1
12) A. Redder, H.W. Becker, J. Görres, M. Hilgemeier, A. Krauss, C. Rolfs, U. Schröder, H.P. Trautvetter, K. Wolke, T.R. Donoghue, T.C. Rinckel and J.W. Hammer, Phys. Rev. Lett. **55** (1985) 1262
13) J.W. Hammer, H.M. Schüpferling, E. Bergandt and Th. Pflaum, Nucl. Instr. Meth. **128** (1975) 409
14) J.W. Hammer, B. Fischer, H. Hollick, H.P. Trautvetter, K.U. Kettner, C. Rolfs and M. Wiescher, Nucl. Instr. Meth. **161** (1979) 189
15) A. Redder, thesis, Universität Münster (1986)
16) S. Seuthe, Diplomarbeit, Universität Münster (1985)
17) J.W. Hammer, G. Bulski, W. Grum, W. Kratschmer, H. Postner and G. Schleussner, Nucl. Instr. Meth. **A244** (1986) 455
18) T. Freye, H. Lorenz-Wirzba, B. Cleff, H.P. Trautvetter and C. Rolfs, Z. Phys. **A282** (1977) 211
19) A. Antilla, J. Keinonen, M. Hantala and I. Forsblom, Nucl. Instr. Meth. **147** (1977) 501
20) H.H. Andersen and J.F. Ziegler, Hydrogen stopping powers and ranges in all elements (Pergamon, 1977)
21) C. Rolfs, Nucleosynthesis – Challenges and new developments, ed. W.D. Arnett and J.W. Truran (University of Chicago Press, 1985) p. 15
22) C.M. Jones, G.C. Phillips, R.W. Harris and E.H. Beckner, Nucl. Phys. **37** (1962) 1
23) P.M. Endt, At. Data and Nucl. Data Tables **23** (1979) 3
24) C. Rolfs, Nucl. Phys. **A217** (1973) 29
25) A.M. Lane and R.G. Thomas, Rev. Mod. Phys. **30** (1958) 257
26) D.C. Weisser, J.F. Morgan and D.R. Thompson, Nucl. Phys. **A235** (1974) 460
27) F.C. Barker, Austral. J. Phys. **24** (1971) 777 and **25** (1972) 341
28) G.J. Clark, D.J. Sullivan and P.B. Treacy, Nucl. Phys. **A110** (1968) 481
29) F.D. Becchetti, D. Overway and J. Jänecke, Nucl. Phys. **A344** (1980) 336
30) W.A. Fowler, G.R. Caughlan and B.A. Zimmerman, Ann. Rev. Astron. Astrop. **13** (1975) 69

31) F.C. Barker, private communication to S.E. Koonin and T.A. Tombrello, and preprint (1986)
32) R. Plaga, Diplomarbeit, Universität Münster (1986)
33) R.A. Baldock, B. Buck and J.A. Rubio, Nucl. Phys. **A426** (1984) 222
34) G.R. Caughlan, W.A. Fowler, M.J. Harris and B.A. Zimmerman, At. Data and Nucl. Data Tables **32** (1985) 197
35) C.A. Barnes, private communication (1986)